Progress In Electromagnetics Research, PIER 61, 67–87, 2006

BISAR MAPPING II. TREATMENT, SIMULATION AND EXPERIMENTATION

M. J. BenKassem and J. Saillard

IREENA – équipe Radar
Ecole Polytechnique de l'Université de Nantes
1 rue C. PAUC 44306 Nantes Cedex 03, France

A. Khenchaf

Centre de Recherche E3I2, ENSIETA
2 rue François Verny, 29806 Brest Cedex 09, France

Abstract—This second part will be devoted to the development of a bistatic synthetic aperture processing method for radar imaging. Indeed, we establish various process that the received signal must undergo in order to estimate the target reflectivity in the bistatic case.

High resolution image is obtained by two treatments on the table image of the bistatic received signal developed in the companion paper.

The detail of the image reconstructing by a BISAR will be presented in this paper. The interest of this model is important, because it permits for a defined scenario generation of radar data which can be used in signal processing algorithms for target detection, identification and mapping.

We present the simulation results for various scenes. These results are obtained by using two algorithms developed for BISAR imagery. Then we present the experimental results.

1. INTRODUCTION

BISAR imagery is developed from phase coherent signal processing of range and Doppler shift measurements. The amplitude and the phase of the received signals are collected for the duration of an integration period after which the data is processed to produce an image of the scene. High range resolution is achieved by the use of wide bandwidth

transmitted pulses. High cross range resolution is achieved by focussing with a signal processing technique, an extremely long antenna that is synthesized from the coherent phase history [1]. The BISAR is thus a system which allows radar images of high resolution.

The receiving signal is detected sequentially pulse by pulse and is stored to be treated. The reconstruction of a high resolution image is obtained by two treatments on the table image of the received signal [2]. The first treatment is a convolution of the received signal by a returned and conjugated transmitted signal. This operation allows a better resolution in range direction. To have a resolution in cross range direction similar to that found in range direction, two methods are used. The first consists of adding in a coherent way all signals scattered by the same pixel when this pixel is crossed by the common lobe of the transmitting and the receiving antennas; this method is called coherent summation. The second method is the well known method of adapted filtering.

2. COHERENT SUMMATION

This method [3] is based on the coherent summation of all signals processed in range direction of the same target when this target is crossed by the common lobe of the transmitting and receiving antennas, (Fig. 1).

A reflectivity estimation of the pixel $M_i(r_i, y_i)$ is given by (1).

$$\begin{aligned}\hat{I}(r_i, y_i) &= \sum_{n=i-\frac{L}{2}}^{i+\frac{L}{2}} S_{r_n cs}\left(\frac{2R_{in}}{c}, y_n\right) \\ &= \iint K(r_i, y_i) G^r S(r_i, y_i) G^e \Gamma_{S_{e_d}}\left(\frac{R_{in}}{c} - \frac{R_n}{c}\right) \\ &\quad \cdot e^{-j\frac{2\pi}{\lambda_0}\chi} e^{j\frac{2\pi}{\lambda_0}\mu_i} \frac{\sin\left[(q+1)\frac{2\pi}{\lambda_0}\frac{\mu}{2}\right]}{\sin\left[\frac{2\pi}{\lambda_0}\frac{\mu}{2}\right]} dr dy \end{aligned} \quad (1)$$

Where: i is the intermediate position for which the transmitter and the receiver see the pixel $M_i(r_i, y_i)$ simultaneously.

L is the number of the transmitting antenna position for which the common lobe illuminates the target. It is given by (2).

$$L = \frac{y_f - y_d}{v_E T_r} \quad (2)$$

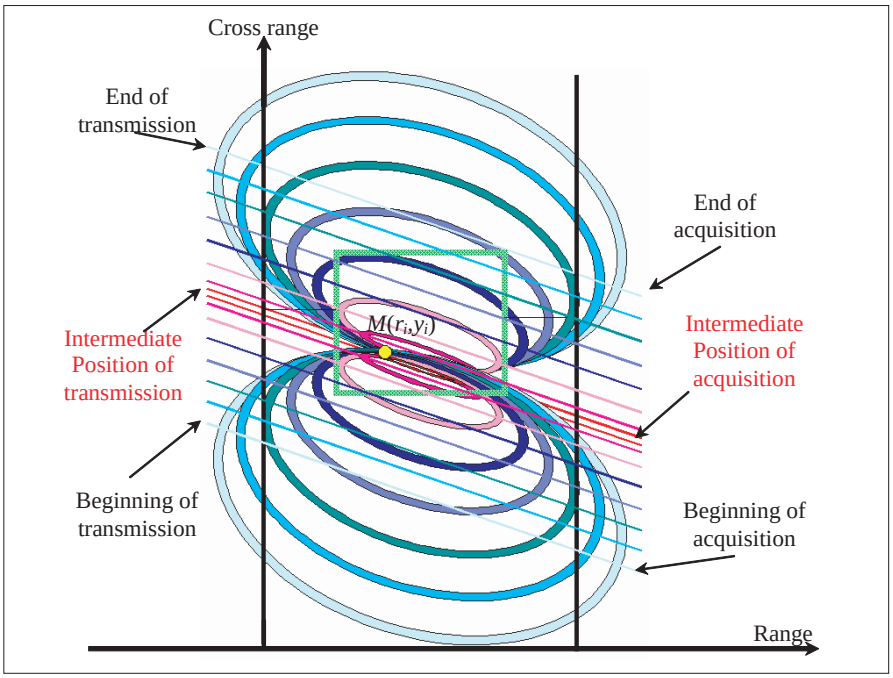

Figure 1. Acquisition geometry.

y_d corresponds to the beginning position of the acquisition,
y_f corresponds to the final position of the acquisition,
$K(r_i, y_i)$ represents the gain of the antenna, the radiation decline, the losses and the gain of the transmission-reception channel,
$S(r_i, y_i)$ is the reflectivity of the surface element $dxdy$,
$\Gamma_{S_{e_d}}$ is the function of ambiguity in the site direction. It is given by (3) [4].

$$\Gamma_{S_{e_d}}\left(\frac{R_{in}}{c}-\frac{R_n}{c}\right)=\left[T-\left|\frac{R_{in}-R_n}{c}\right|\right] \cdot\frac{\sin\left[\pi a\left(\frac{R_{in}-R_n}{c}\right)\left(T-\left|\frac{R_{in}-R_n}{c}\right|\right)\right]}{\pi a\left(\frac{R_{in}-R_n}{c}\right)\left(T-\left|\frac{R_{in}-R_n}{c}\right|\right)} \quad (3)$$

χ, μ, and μ_i are given respectively by (4), (5) and (6):

$$\chi = r - r_i + \frac{1}{2}\frac{y^2 - y_i^2}{r_i^E} + \frac{1}{2}\frac{y^2 - y_i^2}{r_i^R} + \frac{(y - y_i)Y_0}{r_i^R} \tag{4}$$

$$\mu = \left[\frac{(y - y_i)}{r_i^E} + \frac{(y - y_i)}{r_i^R}\right] y_1 \tag{5}$$

$$\mu_i = \left[\frac{(y - y_i)}{r_i^E} + \frac{(y - y_i)}{r_i^R}\right] y_i \tag{6}$$

$\hat{I}(r_i, y_i)$ corresponds well to the estimate of the reflectivity at the point $M_i(r_i, y_i)$.

3. ADAPTED FILTERING

This method uses the azimuth phase term of the received signal which enables us to find the impulse response of the filter adapted to the target $M(Y, d)$ in the cross range direction.

A pixel on the ground will be tracked down (Fig. 2), either by its cartesian coordinates $(x, y, 0)$, or by its coordinates in the oblique plane (r, y), or by its site and azimuth angles with regard to the axis of the antenna (θ, β). An estimation of the reflectivity of the pixel

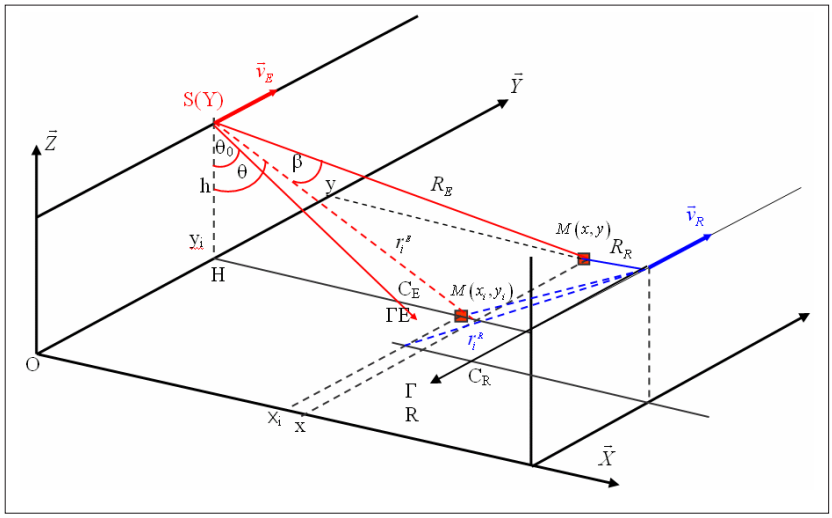

Figure 2. Bistatic configuration.

$M_i(x_i, y_i)$ is given by (7).

$$\hat{I}(Y,d) = S(Y,d) \underset{Y}{\otimes} \Gamma_\mu(Y,d) \underset{d}{\otimes} \Gamma_{\xi_d}(d) \tag{7}$$

$\Gamma_{S_{e_d}}$ is the ambiguity function in the range direction. It is given by (8)

$$\Gamma_{\xi_d}(d) = (cT - |d|) \frac{\sin\left[\dfrac{2\pi ad}{c^2}\left(\dfrac{cT}{2} - \dfrac{|d|}{2}\right)\right]}{\dfrac{2\pi ad}{c^2}\left(\dfrac{cT}{2} - \dfrac{|d|}{2}\right)} \tag{8}$$

Γ_μ is the ambiguity function in the cross range direction. It is given by (10):

$$\Gamma_\mu(Y,d) = 2\vartheta(Y,d) e^{-j\eta y_c} \Delta Y \frac{\sin(\eta \Delta Y)}{\eta \Delta Y} \tag{9}$$

Where

$$\vartheta(Y,d) = g_A^2(Y) e^{j\frac{2\pi}{\lambda_0}\frac{Y^2}{2\left(d-r_0^R\right)}} e^{j\frac{2\pi}{\lambda_0}\frac{2YY_0}{2\left(d-r_0^E\right)}} e^{j\frac{2\pi}{\lambda_0}\frac{Y^2}{2\left(d-r_0^E\right)}} \tag{10}$$

And

$$\eta = \frac{2\pi}{\lambda_0} Y \left[\frac{2d - r_0^E - r_0^R}{\left(d - r_0^E\right)\left(d - r_0^R\right)}\right] \tag{11}$$

4. SIMULATION RESULTS

This section presents the simulation results for various scenes. These results are obtained by using the two algorithms developed for BISAR imagery. Firstly we give the results obtained by the bistatic coherent summation method. Then, we give the estimate of the scene reflectivity by the adapted filtering method. Two types of scenes were selected to apply our simulator.

4.1. Model of Scene Containing Only One Contributor

We carried out simulations which allow to illustrate the geometrical configuration given in Fig. 1. Configuration for which the simulator will be used to make up the map of a scene contain only one isotropic reflector.

The geometry used for the simulation of this model is given in Fig. 3.

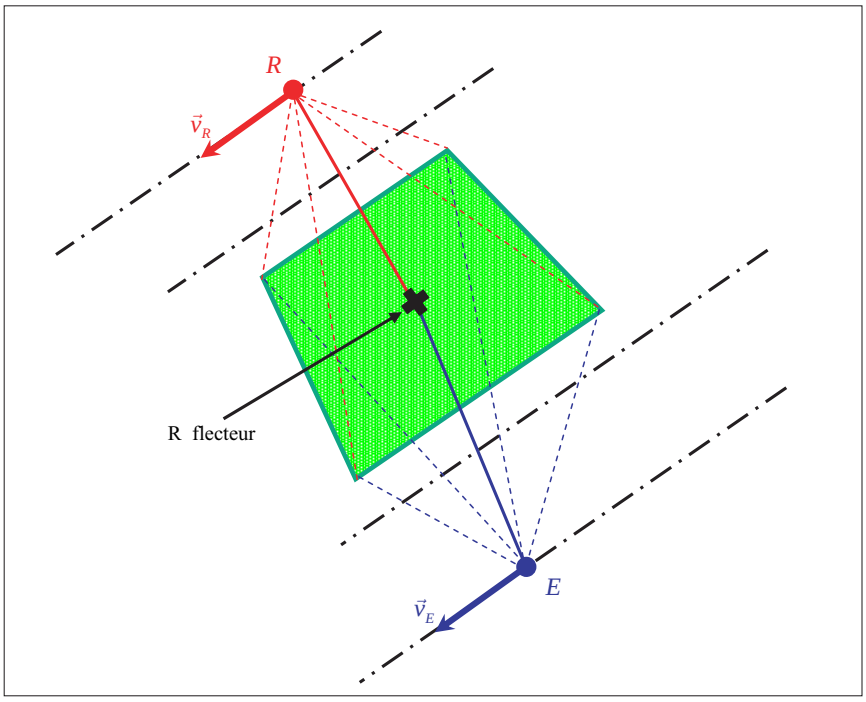

Figure 3. Model of scene containing only one contributor.

The transmitter emits a chirp in the direction of the scene to take on image. The receiver has a field of view programmed in the direction of the scene. It allows the reception of the signals diffused by the common volume of the bistatic radar. In this case, we supposed that the scene consists of only one contributor for which $RCS = 1$.

Fig. 4 illustrates the simulation result. It represents the image rebuilt by the bistatic coherent summation method. On this figure, the peak corresponds to the contributor reflectivity. The simulation results are in agreement with the geometrical and physics predictions due to the bistatic Doppler phenomena. This figure shows the manner by which the BISAR system estimates the reflectivity by the coherent summation method. This manner is particular for each system: bistatic Fig. 4 and monostatic Fig. 5 and Fig. 6.

Fig. 7 presents the reflectivity estimate of the same scene by the adapted filtering method.

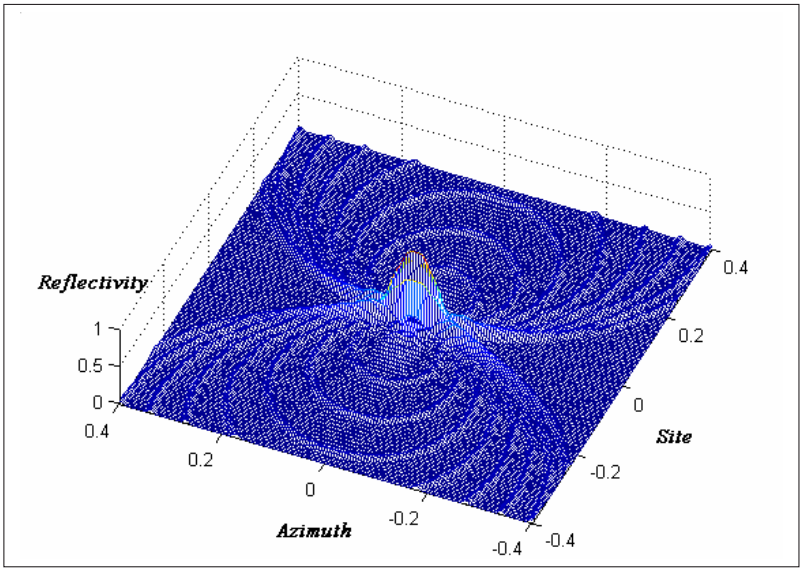

Figure 4. Image reconstructed by bistatic coherent summation method.

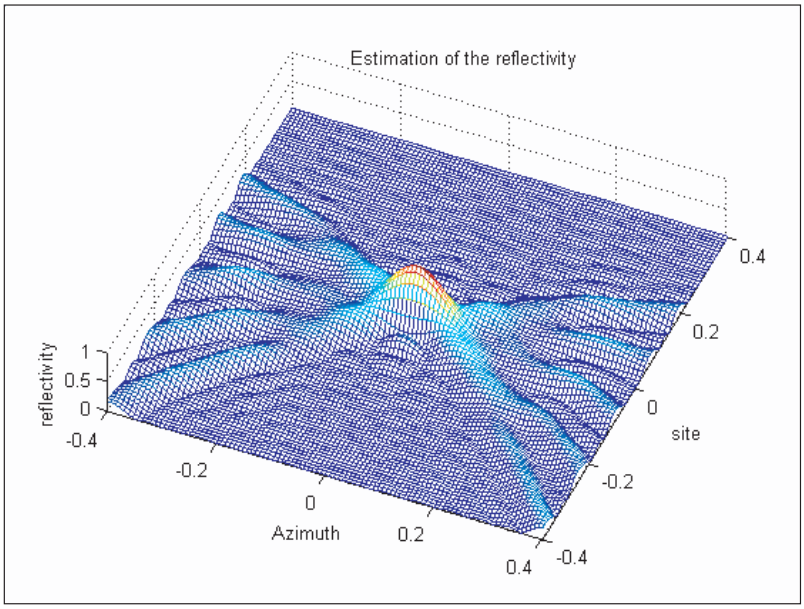

Figure 5. Image reconstructed by monostatic coherent summation method.

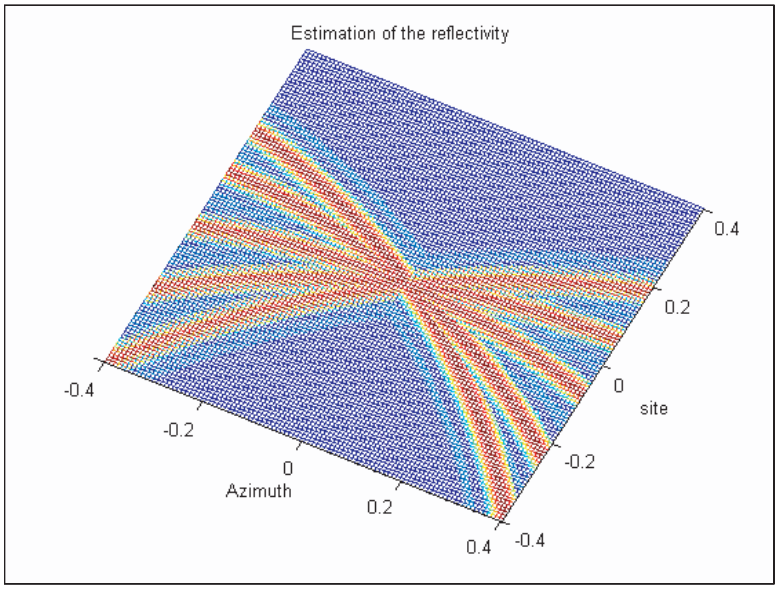

Figure 6. Range-cross range view.

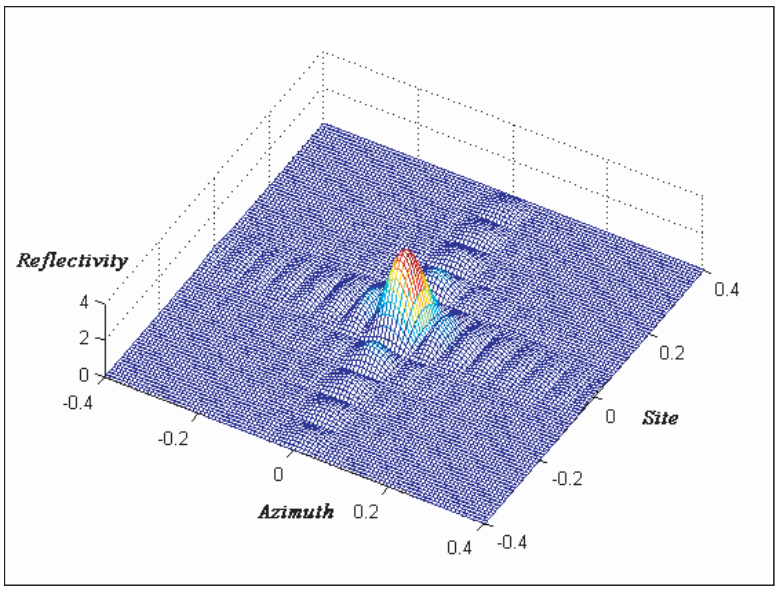

Figure 7. Reconstructed image by bistatic adapted filtering method.

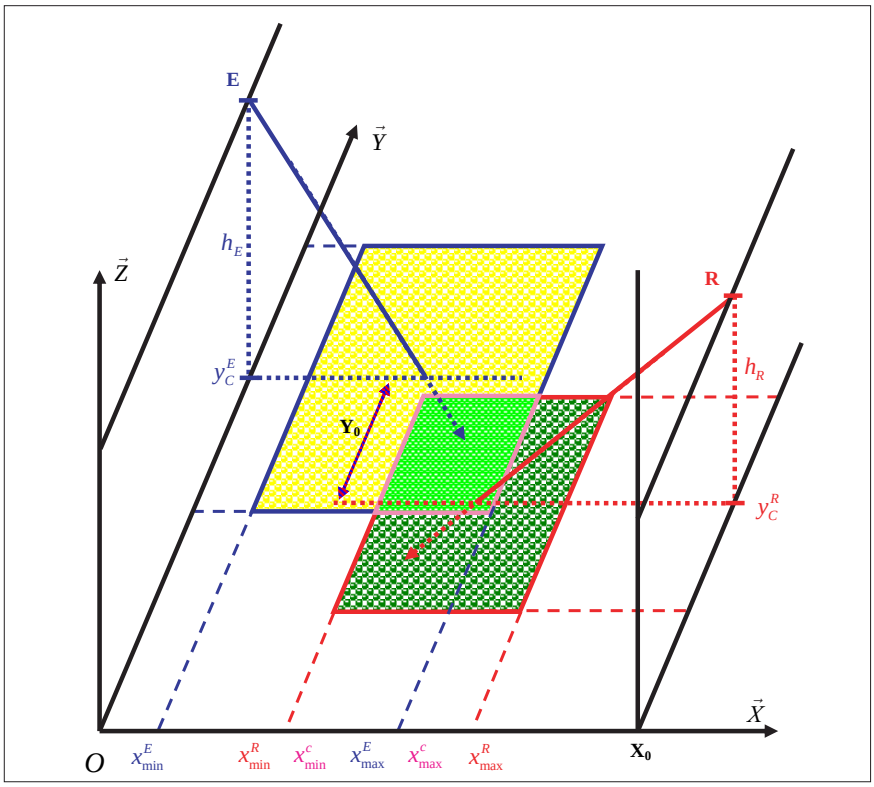

Figure 8. Geometrical configuration.

4.2. Model of Scene Containing Five Isotropic Contributors

The geometry of the system used for simulation is given by Fig. 8. The transmitter and the receiver move in parallel to image the scene supposed plane. The transmitter and the receiver are separated in range direction by a distance equal to 1160 and in cross range direction by a distance equal to 60 m. It is supposed that the transmitter is located at a height equal to 900 m and that the receiver is located at a height equal to 1300 m.

We apply our simulator to a scene made up of five elementary independent and isotropic contributors. The five contributors having the same $RCS = 1$ are geometrically located with respect to the universal set $(O, \vec{X}, \vec{Y})$ as shown in Fig. 9.

Table 1 gives the position of the five contributors in the orthogonal

Table 1. Coordinates of the position contributors in the imaged scene.

$X_{M_i}(m)$ range direction	$Y_{M_i}(m)$ cross range direction
550	520
580	520
610	520
595	505
595	535

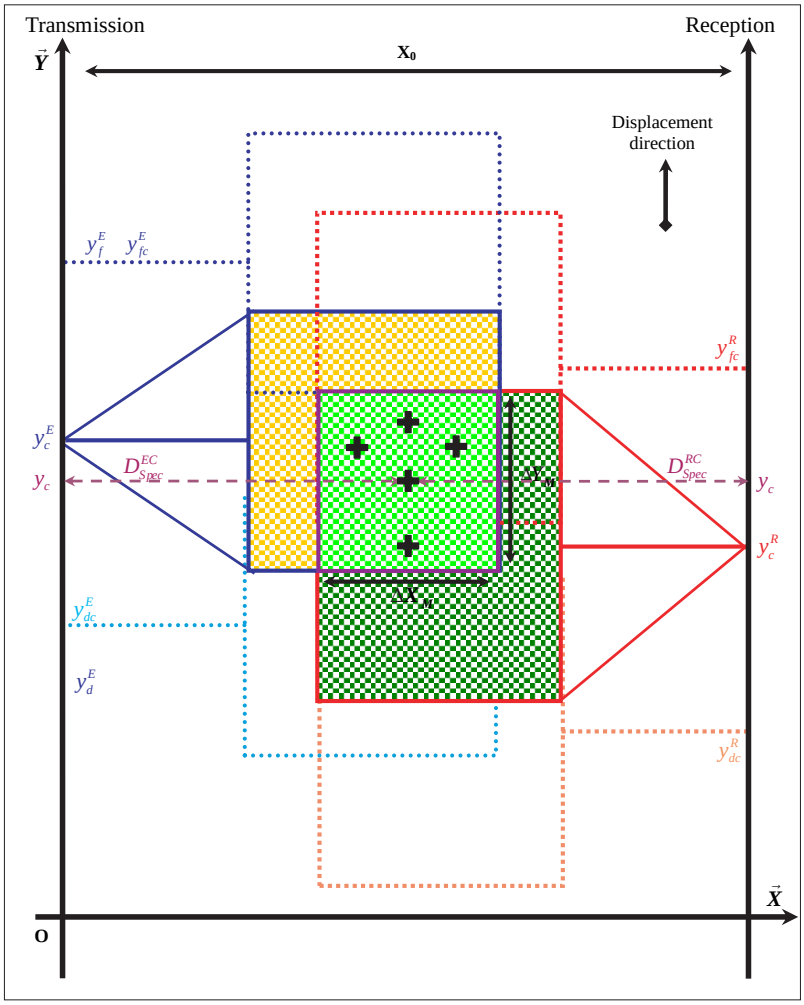

Figure 9. Model of simulation in plane (OX, OY).

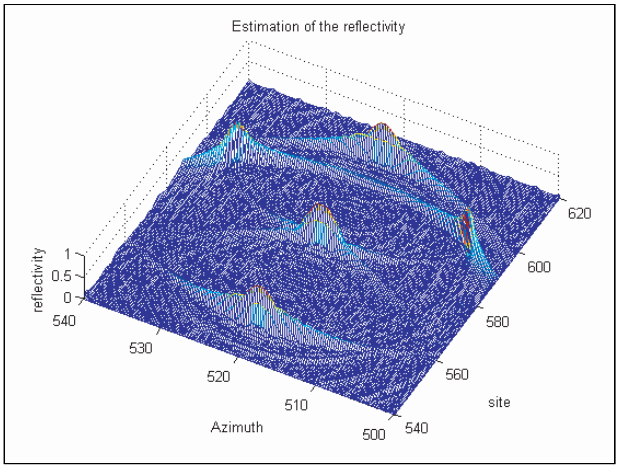

Figure 10. Image reconstructed by bistatic coherent summation method.

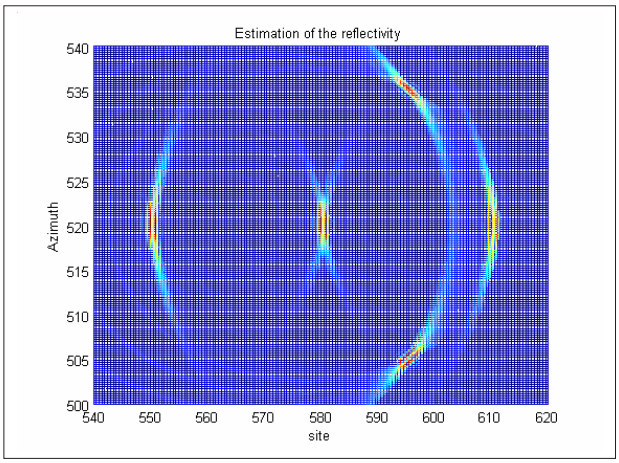

Figure 11. View of the image in the range-cross range plane.

set $(O, \vec{X}, \vec{Y})$.

We present the results obtained by our simulator using the two algorithms developed for BISAR imagery.

Fig. 10 illustrates the simulation result of the scene by the coherent summation method, the five peaks corresponding to the reflectivity of each contributor [5]. Fig. 11 shows the same scene viewed in the range-cross range plane.

The same scene is simulated by the adapted filtering method. The simulation result is illustrated on Fig. 12 and Fig. 13 [5].

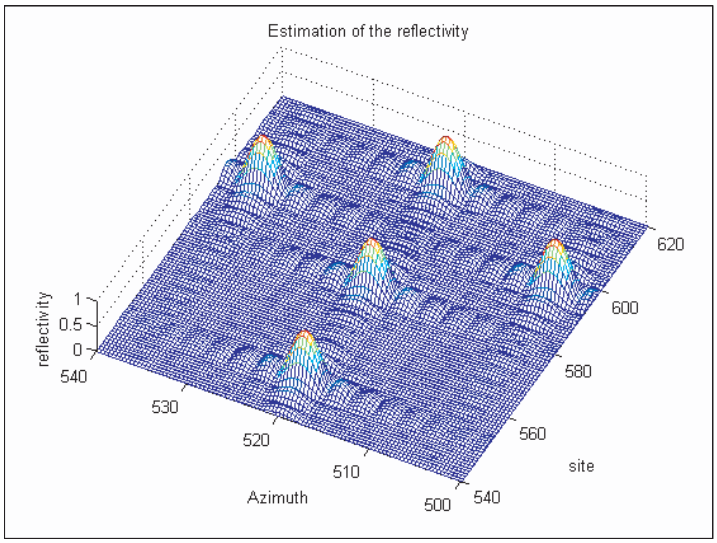

Figure 12. Image reconstructed by bistatic adapted filtering method.

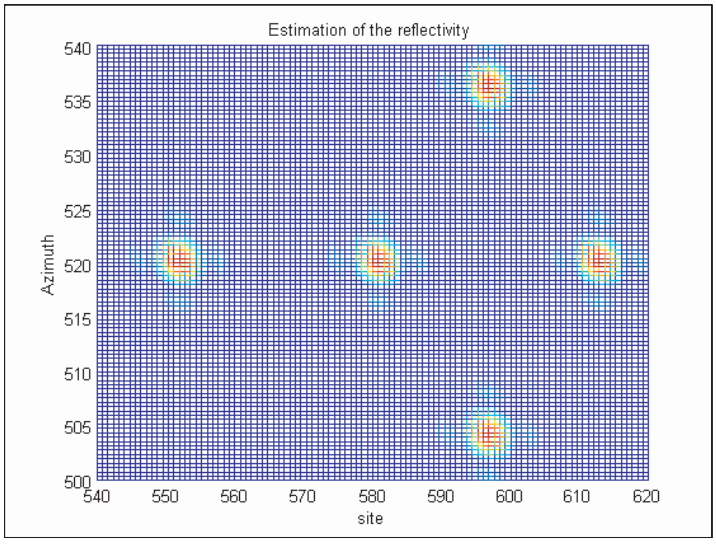

Figure 13. View of the image in the range-cross range plane.

5. EXPERIMENTAL RESULTS

In the previous sections, we developed the theoretical model of a bistatic radar mapping system. In this section, we search to improve a complete BISAR structure. We propose to highlight, starting from a laboratory setting, the fundamental properties of the BISAR system and its advantage compared to the MONOSAR one.

Thus, we applied our method for BISAR mapping in the case of a scene made up of three isotropic individual reflectors. Fig. 14 shows the geometrical configuration.

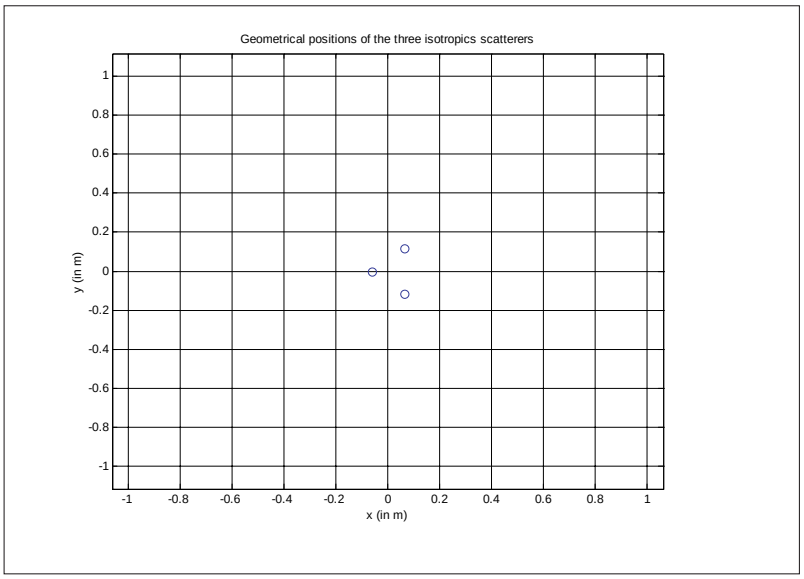

Figure 14. Geometrical positions of the three spherical isotropic scatterers used for real data acquisition.

Our simulator made the radar image of the scene viewed by two angular fields $[-4°, +4°]$ and $[+86°, +94°]$ respectively. The results of this simulation show the way in which the system views the scene for these two preset angular fields

Fig. 15 illustrates the reconstructed map of the scene for $[-4°, +4°]$ angular field view.

Fig. 16 illustrates the reconstructed map of the scene for $[+86°, +94°]$ angular field view.

Real data was obtained in the anechoic chamber of ENSIETA (*Brest, France*) for three spherical isotropic scatterers, made by 30 mm metallic spheres and positioned as shown in Fig. 17. It illustrates our

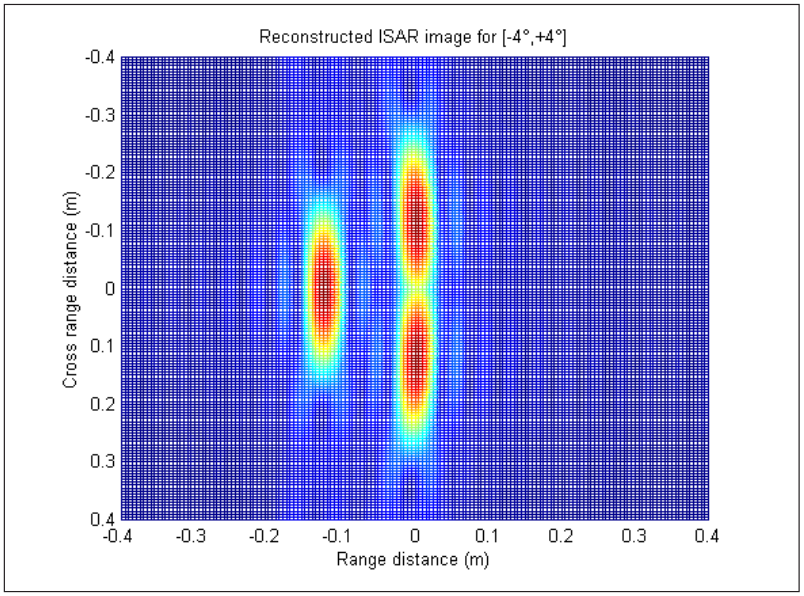

Figure 15. 2D radar image of the target for 0° presentation angle.

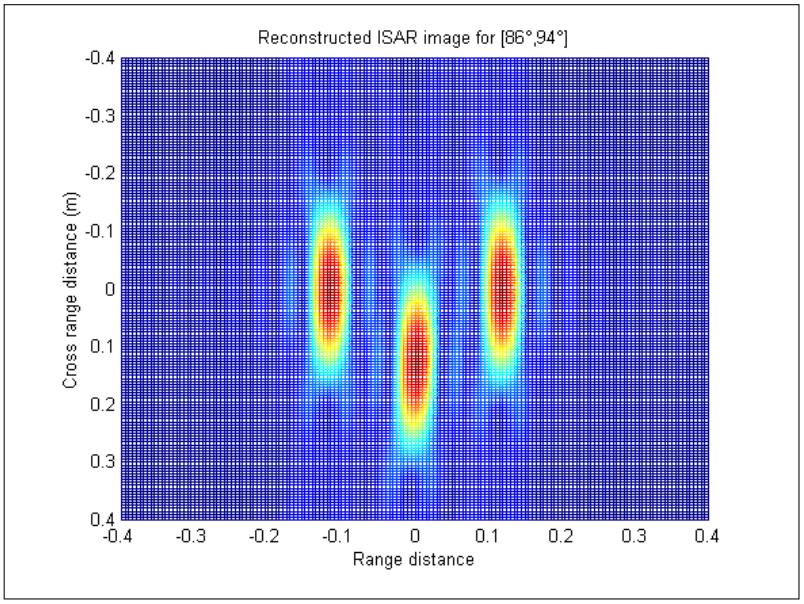

Figure 16. 2D radar image of the target for 0° presentation angle.

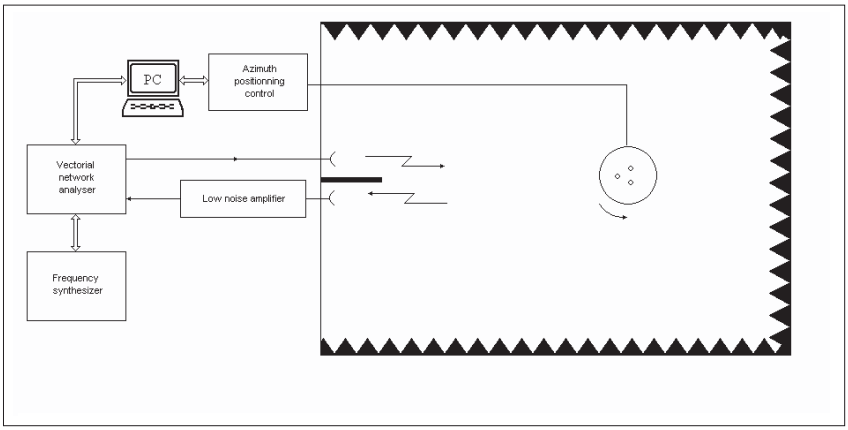

Figure 17. Experimental set-up.

measurement system. This system is controlled by a PC which allows a very smooth operation using the Labview software.

The vectorial network analyzer is a WILTRON 360 type and it can operate in 10 MHz–18 GHz range. This analyzer controls the frequency synthesizer and guides the generated signal to the Cornet antenna (*2 GHz–18 GHz effective range*). The reflected signal is received with an identical antenna and is amplified with an MITEK low noise amplifier (*6 GHz–18 GHz effective range*).

The amplitudes and phases achieved by quadrature demodulation in the vectorial network analyzer are transmitted to the PC where they are recorded.

The computer also controls the NEWPORT positioning system which has an 0.01 degree angular resolution. This positioning system supports the polystyrene

The positioning system and the walls of the anechoic chamber are covered with radio absorber material. A radio absorber panel is also placed between the antennae to decrease their coupling

The distance between the antennae and positioning system is 6 m, and the anechoic chamber dimensions are $8 \times 5 \times 5\text{m}^3$.

A frequency stepped signal was used in the acquisition phase. Each data snapshot has been obtained for 128 frequency steps of $\Delta f = 50\,\text{MHz}$, uniformly swept over the band $B = [11.65; 18]$ GHz. Consequently, the slant range resolution and ambiguity windows are given by:

$$\begin{aligned} \Delta R_S &= c/2B = 2.3\,\text{cm} \\ W_S &= c/2\Delta f = 3\,\text{m} \end{aligned}$$

The target was successively illuminated on two angular excursions equal to 8 degrees intervals centred respectively on 0° and 90° target presentation angles, and with an angular increment of $\Delta\alpha = 0.5°$. Thus, the cross-range resolution and ambiguity window are given by:

$$\begin{aligned} \Delta R_T &= \lambda_{mean}/2\Omega = 7.2\,\text{cm} \\ W_T &= \lambda_{mean}/2\Delta\alpha = 1.14\,\text{m} \end{aligned}$$

All these experimental conditions are reported in Table 2.

Table 2. Experimental conditions.

Target diameter	30 mm
Frequency band	$B = [11.65; 18]$ GHz
Frequency increment	$\Delta f = 50$ MHz
Range resolution	$\Delta R_S = c/2B = 2.3$ cm
Range ambiguity window	$W_S = c/2\Delta f = 3$ m
Angular excursion	$\Omega = [-4°; +4°]$ and $\Omega = [86°; 94°]$
Angular increment	$\Delta\alpha = 0.5°$
Cross-range resolution	$\Delta R_T = \lambda_{mean}/2\Omega = 7.2$ cm
Cross-range ambiguity window	$W_T = \lambda_{mean}/2\Delta\alpha = 1.14$ m
Scatterers coordinates (relative to the rotation axis, in meters)	$\begin{pmatrix} -0.125 \\ 0 \end{pmatrix}$; $\begin{pmatrix} 0 \\ 0.1175 \end{pmatrix}$; $\begin{pmatrix} 0 \\ -0.1175 \end{pmatrix}$

Fig. 18 illustrates the ISAR imaging processing when using a stepped frequency (*SF*) waveform [21].

The radar transmits a sequence of N bursts. Each burst consists of M narrow band radio pulses. Within each burst, the center frequency $\boldsymbol{f_m}$ of each successive pulse is increased by a constant step $\boldsymbol{\Delta f}$. The total bandwidth of the burst, i.e., M times the frequency step $\boldsymbol{\Delta f}$, determines the radar range resolution. The total number of bursts N for given imaging time duration determines the Doppler or cross-range resolution. The returned pulse is heterodyned and quadrature detected in the radar receiver. To form a radar image, after measuring the returned in-phase (*I-channel*) and quadrature-phase (*Q-channel*) signals at base band with a pulse repetition rate at $M \times N$ time instants $\boldsymbol{t_{m,n} = (m + n \cdot M) \cdot \Delta t}$, the M by N complex data are organized into a 2-D array which represents the

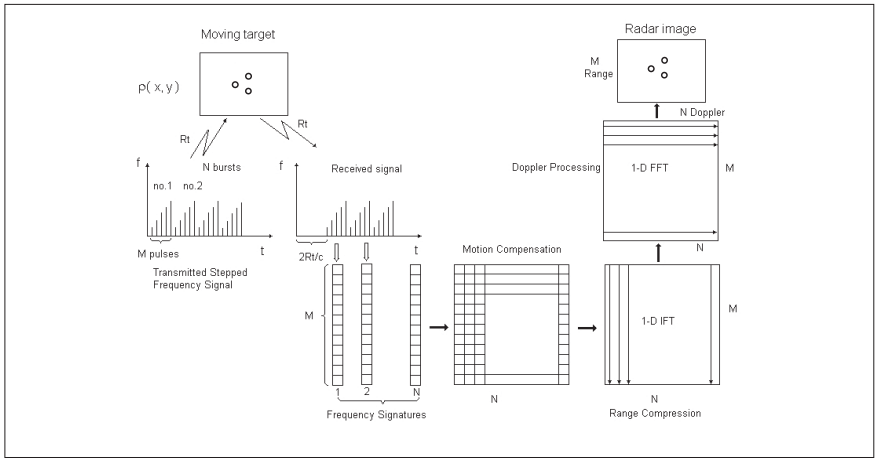

Figure 18. Stepped frequency radar imaging of moving target.

unprocessed spatial frequency signature of the target $\boldsymbol{S(f_{m,n})}$ where $\boldsymbol{m = 0 \ldots M-1,\ n = 0 \ldots N-1}$ and $\boldsymbol{\Delta t}$ denotes time interval between pulses.

The radar processing algorithm uses the frequency signatures as the row data to perform range compression and the standard motion compensation.

For the Stepped-Frequency signals, the range compression performs an M-point Inverse Fourier Transform for each of the N received frequency signatures as:

$$G(r_{m,n}) = IFT_m\{S(f_{m,n})\} \tag{12}$$

IFT_m denotes the Inverse Fourier Transform operation with respect to the variable m.

Therefore, N range profiles (*i.e., the distribution of the target reflective points in range*), each containing M range cells, can be obtained. At each range cell, the N range profiles constitute a new time history series. Then, the motion compensated range profiles become $\boldsymbol{G'(r_{m,n})\ m = 0 \ldots M-1,\ n = 0 \ldots N-1}$. Note: for our experimental conditions, this motion compensation processing is not necessary.

The Fourier imaging approach takes the fast Fourier transform of the time history series and generates an N point Doppler spectrum, as Doppler profile.

By combining the N Doppler spectra at M range cells, finally, the

M by N image is formed:

$$I(r_m, f_n) = FFT_n\{G'(r_{m,n})\} \tag{13}$$

Therefore, the radar image $\boldsymbol{I(r_m, f_n)}$ is the target's reflective points mapped onto the range-Doppler plane [22].

Because the target is illuminated under a discrete angular range and with a discrete frequency set, the complex measured samples are in polar coordinates.

The 2-D Fourier transform can be applied to the data set only if the sampling of the arguments is uniform. This is true in polar coordinates (θ, f), but is not in the rectangular coordinates system, as it can be observed in Fig. 19. So, it is necessary to interpolate the initial data for achieving an artificial sampling set in a rectangular (k_x, k_y) coordinates system. Then, the radar target image is obtained when the 2-D Fourier transform is applied to the interpolated data.

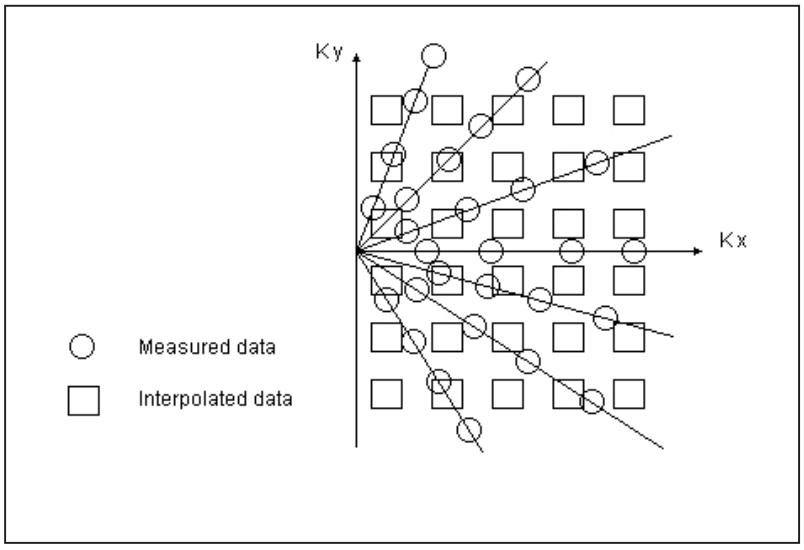

Figure 19. Measured data in polar coordinates and interpolated data in cartesian coordinates.

This two dimensional Fourier processing was used to reconstruct the 2D radar image of the target described above and the results are presented on Fig. 20 and Fig. 21.

Fig. 20 and Fig. 21 illustrate experimental reconstructed map of the scene respectively for $[-4°, +4°]$ and $[+86°, +94°]$ angular field view. Thus, the experimental results are in agreement with our simulator results for the same configuration.

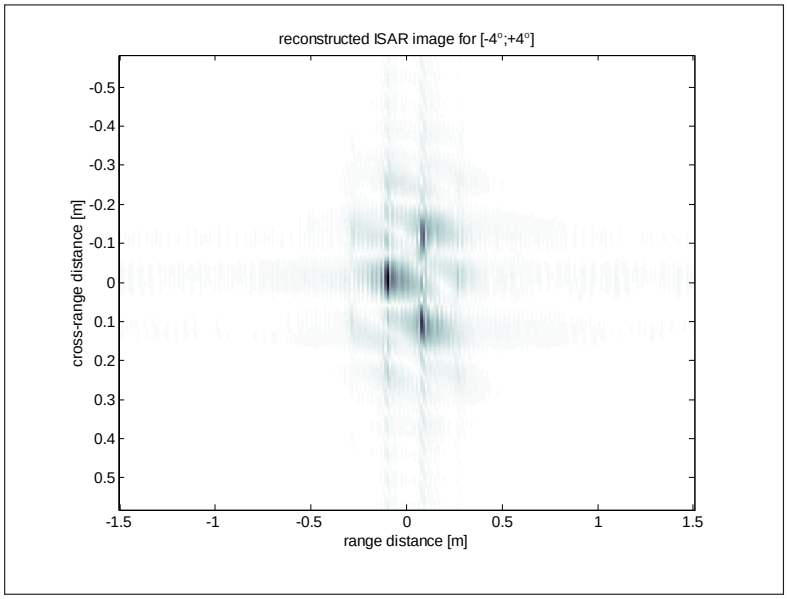

Figure 20. 2D radar image of the target for 0° presentation angle.

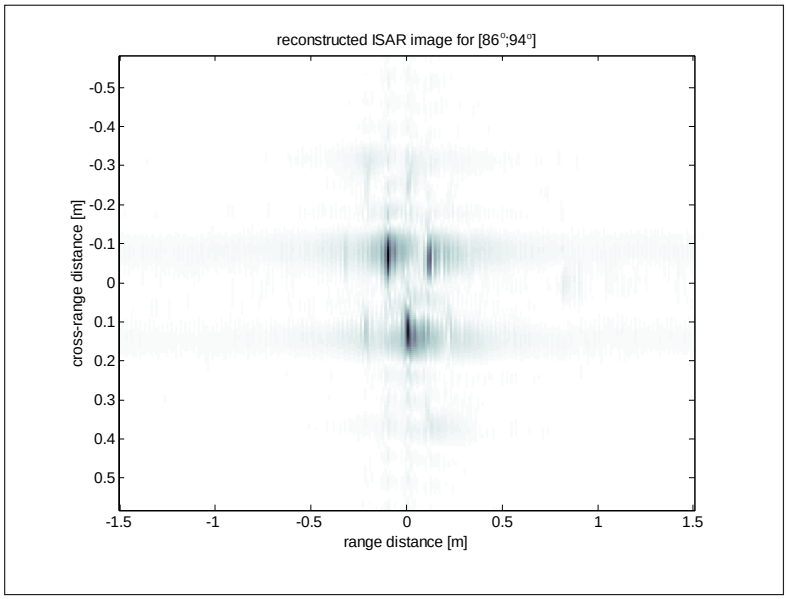

Figure 21. 2D radar image of the target for 90° presentation angle.

6. CONCLUSION

In this paper, various processing, which the received signal must undergo to be able to estimate the reflectivity, are established in the bistatic case.

The signal received by a polarimetric bistatic radar is given in the companion paper. This signal is expressed according to the field scattered by the target, it is also given like a voltage detected at the receiving antenna, function of parameters of the antennae and the geometrical parameters of the transmitting-receiving channel.

Simulations are carried out by using two methods of image reconstruction : coherent summation and adapted filtering. Experimental results are in agreement with our simulator results.

A bistatic mission allows the simultaneous acquisition of two samples of the target scattering pattern, opening the way to new research activities concerning, for example, sea and water surface studies and land cover classification.

Consequently, the observation under two different angles allows to view, in a bistatic image, areas of reflection which are dark in a monostatic SAR image or to improve spectral surface analysis combining two images. We can also improve spectral surface analysis combining two images [8].

The acquisition of two images of the same area under different angles, also gives the capability of obtaining digital elevation models.

Bistatic missions allow the simultaneous acquisition of multifrequency, multipolarisation, and, in particular, multiangle data sets ; the statistical analysis allows also the improvement of the correct classification probability.

The interest of this model is great because it permits, for a defined scenario generation of radar data which can be used in signal processing algorithms for target detection and mapping.

REFERENCES

1. Soumekh, M., *Synthetic Aperture Radar Signal Processing*, Wiley-Interscience Publication, United States of America, 1999.
2. El Assad, S., I. Lakkis, and J. Saillard, "Holographic SAR image formation by coherent summation of impulse response derivatives," *IEEE Transactions on Antennas and Propagation*, Vol. 41, No. 5, 620–624, May 1993.
3. El Assad, S., I. Lakkis, and J. Saillard, "Holographic SAR image formation by coherent summation of impulse response

derivatives," *IEEE Transactions on antennas and Propagation*, Vol. 41, No. 5, 620–624, May 1993.

4. BenKassem, M. J. and A. Khenchaf, "Bistatic mapping radar BISAR," *OCEANS*, San Diego, USA, September 22–26, 2003.
5. BenKassem, M. J., J. Saillard, and A. Khenchaf, "BISAR mapping, modeling and processing," *European Conference on Propagation and Systems*, Brest, March 2005.
6. Radoi, E., "Automatic target recognition using range profiles," Ph.D. Thesis, 1999.
7. Chen, V. C. and S. Qian, "Joint time frequency transform for radar range-doppler imaging," *IEEE Trans. Aerospace and Electronic Systems*, Vol. 34, No. 2, 486–499, 1998.
8. Hanle, E., "Fundamental problems of bistatic and multistatic radar," *Conference on Modern Radar Problems*, 74–83, Zakopane, Pologne, 1983.